Scripta Materialia 242 (2024) 115962

Contents lists available at ScienceDirect

Scripta Materialia

journal homepage: www.journals.elsevier.com/scripta-materialia

Microstructure and thermal stability of crystalline/amorphous Fe/FeW nanomultilayers

K. Russell [a], C. Killeen [b], N.J. Peter [c], R. Schwaiger [c], J.R. Trelewicz [b,d], A.M. Hodge [a,e,*]

[a] Department of Chemical Engineering and Materials Science, University of Southern California, Los Angeles, CA 90089, USA
[b] Department of Materials Science and Chemical Engineering, Stony Brook University, Stony Brook, NY 11794, USA
[c] Institute for Energy and Climate Research, Structure and Function of Materials (IEK-2) Forschungszentrum Jülich GmbH, Jülich 25425, Germany
[d] Institute for Advanced Computational Science, Stony Brook University, Stony Brook, NY 11794, USA
[e] Department of Aerospace and Mechanical Engineering, University of Southern California, Los Angeles, CA 90089, USA

ARTICLE INFO

Keywords:
Multilayers
Amorphous alloys
Thermally activated processes
Interfaces
Recrystallization

ABSTRACT

The thermal stability of crystalline-amorphous interfaces was investigated in Fe/FeW nanomultilayers (NMs), where the alloy layers were amorphous in the as-sputtered state with concentrations of Fe-38 at.% W or Fe-67 at.% W. Compositionally driven devitrification, layer breakdown, and recrystallization were compared using both single-layer and multilayer configurations at temperatures ranging from 250 °C to 750 °C. Annealing of the NMs to 500 °C revealed destabilization in the Fe-67 W layers with the formation of crystalline-crystalline interfaces (CCIs) whereas the Fe-38 W layers remained intact with stable crystalline-amorphous interfaces (CAIs). Further annealing to 750 °C resulted in multilayer evolution and recrystallization, where breakdown of the CAIs was attributed to layer intermixing while the CCIs experienced intermetallic grooving and pinch-off. The influence of amorphous stability, composition, and intermetallic formation are discussed with respect to the NM breakdown mechanisms. This work highlights a promising strategy for exploring compositionally driven stability at the nanoscale in crystalline-amorphous alloys.

Metallic nanomultilayers (NMs) are thin film coatings consisting of alternating nanometric metallic layers that can be tailored to control composition, interface energy, and layer structure [1]. These materials have exhibited exceptional mechanical, optical, magnetic, and irradiation resistant properties, which are generally attributed to nanoscale features [2]. Furthermore, NMs can be readily tuned to alter film properties, thus providing convenient model systems for investigating fundamental mechanisms governing stability of nanostructured materials [3], such as the effects of interfacial energy and solute segregation [4]. For example, pseudomorphic growth has been used to reduce interface energy and in turn improve thermal stability, but such a technique generally consists of NMs with ultrathin layers (<5 nm) [5–7]. For many systems, grain growth can be mitigated via kinetic and thermodynamic stabilizing mechanisms. Zenner pinning reduces grain boundary mobility whereas solute segregation via doped grain boundaries (DGBs) lowers interfacial free energy, thereby suppressing the overall driving force for coarsening [8]. Efforts have focused on modeling candidate material systems capable of solute segregated stabilization [9–11] and experimental verification [12–15] including the use of NMs to explore the implications of temperature dependent segregation [16].

Recent findings observed the formation of amorphous intergranular films (AIFs), often referred to as amorphous complexions, at extreme temperatures that significantly improve the thermal stability of the nanocrystalline state [17–19]. Formation of nanometer-scale disordered films occurred within DGBs and is postulated to further reduce grain boundary energy, thereby mitigating grain growth for particular alloy systems [20]. Additionally, alloys containing AIFs displayed improved irradiation damage resistance, largely attributable to the inherent excess free volume within amorphous films and at the crystalline-amorphous interfaces (CAIs) providing energetically favorable sites to accommodate defects [21]. Therefore, interface engineering and incorporation of amorphous phases within NMs offer a potential route towards tailoring alloy stability in extreme environments including high temperature and irradiation [22]. However, current understanding of stability within NMs containing CAIs is largely restricted to metallic/ceramic and ceramic/ceramic systems [16,23]; the few studies on nanometallic systems containing amorphous complexions convolute solute segregation

---

* Corresponding author at: Department of Chemical Engineering and Materials Science, University of Southern California, Los Angeles, CA 90089, USA.
E-mail address: ahodge@usc.edu (A.M. Hodge).

https://doi.org/10.1016/j.scriptamat.2023.115962
Received 20 September 2023; Received in revised form 29 November 2023; Accepted 27 December 2023

and CAI formation. Consequently, there is a gap in the scientific understanding of how crystalline and amorphous-metallic phases influence stability in NM systems containing a high volumetric density of CAIs.

In this work, NMs consisting of alternating nanocrystalline-Fe and amorphous-FeW layers are co-sputtered to identify the influence of CAIs on temperature-driven stability across two multilayer systems. Amorphous layer compositions are deposited as Fe-38.0 at.% W or Fe-67.2 at.% W, which will be referred to henceforth as 'Fe-38W' and 'Fe-67W'. A methodology is presented for investigating NMs containing amorphous metallic phases and assessing how CAIs influence microstructural stability with results revealing compositional dependence of amorphous layers on overall NM stability.

In order to assess the stability of individual compositions, monolithic amorphous films were deposited by direct current (DC) magnetron sputtering inside a vacuum chamber evacuated to a base pressure of 5.0 $\times 10^{-4}$ Pa onto quartz substrates to a nominal thickness of 1000 nm. Magnetron powers ranged from 35 to 60 W for Fe and 50–100 W for W, with a 6.7 $\times 10^{-1}$ Pa working pressure of ultra-high pure grade argon; deposition rates ranged between 2.93 – 4.63 nm/min for Fe and 2.90 – 6.02 nm/min for W. FeW compositions were tuned by controlling powers applied to Fe (99.95 at.% Fe) and W (99.9 at.% W) targets to achieve the compositions summarized in Table 1. These compositions were selected following Lu et al. [24], which reported Fe_xW_{100-x} coatings with 30 at.% $< x <$ 80 at.% could produce amorphous phases but presented limited data on thermal stability.

The as-sputtered and annealed monolithic films were characterized using X-ray diffraction (XRD) on a Bruker D8 Advance X-ray diffractometer and selected area electron diffraction (SAED) with an FEI Talos-F200C-G2 microscope. TEM lamellae were prepared using Helios G4 and G5 PFIB UXe-DualBeam FIB/SEMs. Annealing was conducted at 250 °C, 500 °C, and 750 °C inside a GSL1100X tube furnace (MTI Corporation) for 96 h at 5 $\times 10^{-5}$ Pa.

The XRD profiles for as-sputtered and heat-treated monolithic samples in Fig. 1 show diffuse peaks prior to heat treatment indicating that both as-sputtered films were X-ray amorphous [25]. Inset SAED (100 nm diameter) patterns of the as-sputtered samples exhibited overlapping diffuse diffraction rings and halos, consistent with XRD results. However, subtle diffraction spots within the Fe-67 W SAED pattern suggest nanoscale precipitation but with inadequate intensity to resolve these phases. Prior research on several amorphous alloys observed similar XRD and SAED results, identifying signatures consistent with a predominantly amorphous state with dispersed crystalline regions on the order of several nanometers [26–28]. Therefore, both as-sputtered FeW compositions are classified as "X-ray amorphous" with the Fe-38 W film showing a higher degree of amorphization than the Fe-67 W film.

Table 1
Sample film characteristics and labeling for both single layer and multilayer coatings, including coating thickness, layer and global composition, and number of total bilayers.

Table 1

Sample Name	Coating Type	Coating Thickness [nm]	Layer 1 Fe (20 nm)	Layer 2 FeW (20 nm)	Number of Bilayers	Global Fe Content [at.% Fe]
Fe-38W	Single Layer	1000	N/A	N/A	N/A	62.0 at.% Fe
Fe-67W	Single Layer	1000	N/A	N/A	N/A	32.8 at.% Fe
Fe/Fe-38W	Multilayer	1520	99.9 at.% Fe	67.2 at.% Fe	38	81.0 at.% Fe
Fe/Fe-67W	Multilayer	1520	99.9 at.% Fe	38.0 at.% Fe	38	66.4 at.% Fe

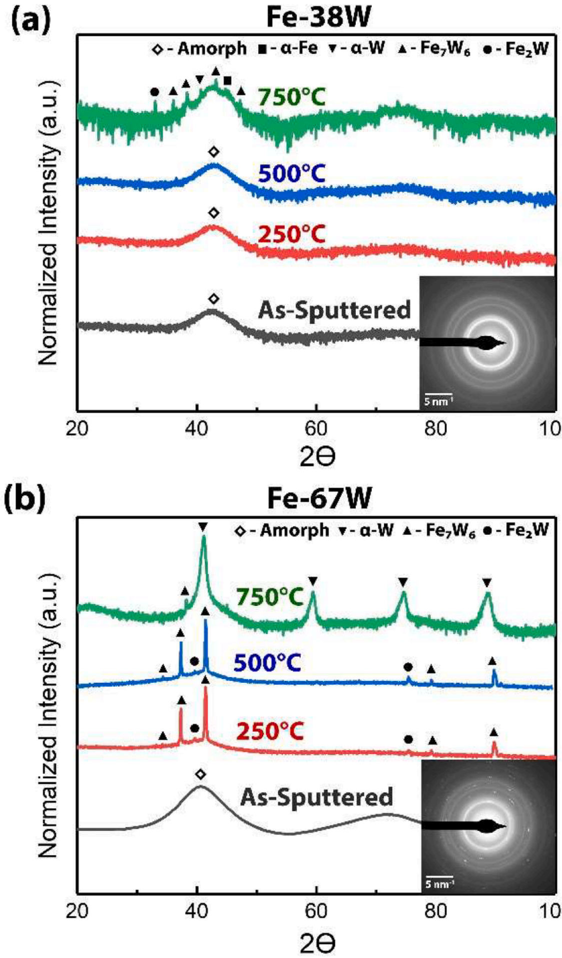

Fig. 1. Normalized *ex-situ* XRD intensity profiles in a logarithmic scale of the as-sputtered and heat-treated temperatures for both single-layer films (a) Fe-38 W and (b) Fe-67 W. Each intensity profile is labeled with its annealing temperature and crystalline peaks are indicated with respective symbols. Inset SAED images of each as-sputtered film show diffraction rings and diffuse halos.

XRD patterns for the annealed monolithic films exhibited different behavior for the two alloy compositions. Following heat-treatment at 250 °C, the Fe-38 W XRD pattern retained its diffuse peak while the Fe-67 W profile contained intense peaks primarily associated with Fe_7W_6 along with a small Fe_2W signature. The emergence of intermetallic peaks combined with the absence of diffuse scattering indicates the Fe-67 W film completely crystallized at 250 °C. Within amorphous metallic alloys, ordered regions can promote thermally induced devitrification and intermetallic formation [29]. The predominance of Fe_7W_6 is consistent with the Fe-W phase diagram [30], though there are uncertainties in the W-rich region of this system [30,31]. After heat-treatment to 500 °C, both Fe-38 W and Fe-67 W XRD plots maintained similar peak profiles observed at 250 °C, indicating no significant coarsening or phase transitions. Annealing at 750 °C produced low-intensity peaks in the Fe-38 W film attributed to α-Fe, α-W, Fe_7W_6, and Fe_2W phases as indexed in Fig 1a, where the minor intermetallic presence is consistent with annealing studies of electrodeposited Fe-W alloys of similar composition [32]. However, convolution of these peaks with the diffuse amorphous signature demonstrates the Fe-38 W alloy did not completely devitrify at 750 °C and instead exhibited exceptional stability relative to many binary and multicomponent metallic glasses [33]. Comparatively, the Fe-67 W film experienced decomposition of the intermetallic phases (Fe_7W_6 and Fe_2W) into a body-centered cubic (BCC) α-W solid solution at 750 °C.

To investigate how CAIs influence microstructural stability, multilayers comprised of repeating nanocrystalline Fe and either Fe-38 W or

Fe-67 W compositions, hereafter referred to as Fe/Fe-38 W and Fe/Fe-67 W, were synthesized through co-sputtering techniques (Table 1). These samples provide a CAI analogue to multilayers with crystalline-crystalline interfaces (CCIs), such as Mo-Au, Hf-Ti, and W-Cr, where microstructural transitions were impacted by excess free energy and pinning forces imparted by CCIs [3]. For the two NM configurations studied here, the global multilayer compositions notably differ from the monolithic amorphous counterparts, as introduction of pure Fe layers increases overall Fe content. Fig 2 highlights the as-sputtered NMs and corresponding microstructural and chemical analysis including high-angle annular scanning transmission electron microscopy (HAADF-STEM), nanobeam electron diffraction (NBED), and energy dispersive X-ray spectroscopy (EDX), implemented using FEI Titan 80–200 ChemiSTEM, JEOL JEM-2100F TEM, and FEI TALOS Operando S/TEM microscopes all operated at 200 keV. Cross-sectional HAADF-STEM micrographs in Fig. 2a and e reveal Fe (dark) and FeW (bright) layers based on the Z-contrast via high-angle scattering (semi-collection angle of 69 – 200 mrad). Magnified STEM micrographs are shown in Fig. 2b and f for Fe/Fe-38 W and Fe/Fe-67 W NMs, respectively, with accompanying NBED patterns from Fe (red) and FeW (blue) layers.

NBED patterns from the Fe layer in both samples exhibit clear diffraction spots deriving from grains of specific crystallographic orientation while the FeW layers show different characteristics depending on the composition. For the Fe/Fe-38 W NM, diffuse halos and a small number of distinct diffraction spots are found in the NBED patterns (Fig. 2b (blue)) where FeW layers are of amorphous character with some possible crystallinity on the order of the beam diameter, about 3 nm. Conversely, for the Fe/Fe-67 W NM, the NBED pattern in Fig. 2f (blue) contained only subtle diffuse diffraction rings with more conspicuous diffraction spots, indicating the presence of more developed crystallites in the Fe-67 W layers. Chemical analysis via EDX is presented in Figs. 2c and 2 g with labeled Fe (red)_and W (blue). These maps demonstrate a clear partitioning of the pure Fe and FeW layers, and line scans following the inscribed arrows show the Fe content fluctuating between 58 and 98 at.% for Fe/Fe-38 W and 32–96 at.% for Fe/Fe-67 W. Overall, characterization of as-sputtered NM samples demonstrates that the FeW layers in the Fe/Fe-38 W NMs are predominantly amorphous but with signatures from nanoscale crystallites, while the Fe/Fe-67 W NMs contained amorphous signatures with a higher degree of crystallinity.

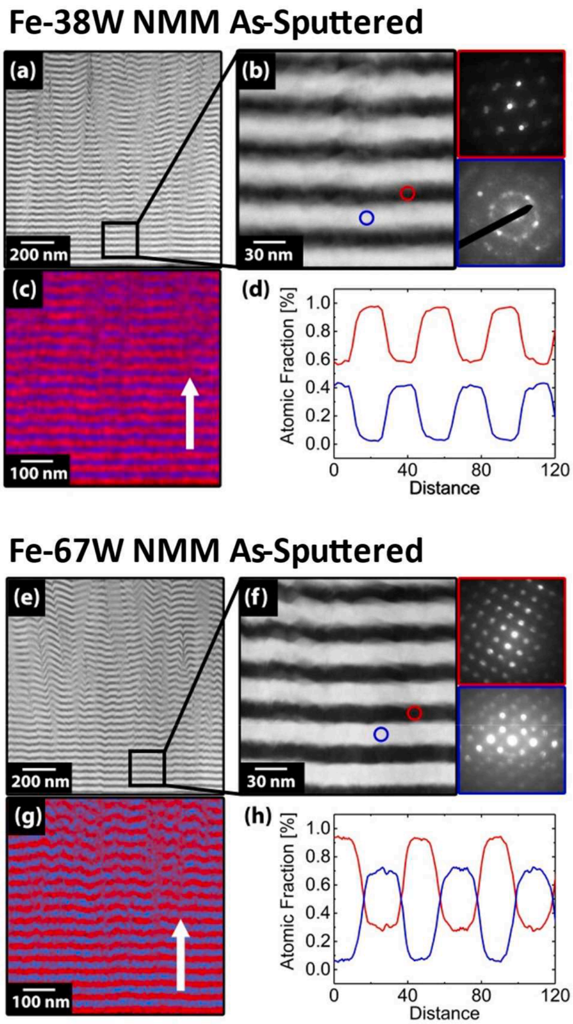

Fig. 2. Microstructural and chemical characterization of as-sputtered (a-d) Fe-38 W multilayer and (e-h) Fe-67 W multilayer films. Microstructural analysis for both samples consists of (a,e) cross-sectional HAADF-STEM micrographs and (b,f) NBED scans with layer locations labeled within magnified STEM images. Chemical investigation consists of (c,g) EDX mapping of film cross sections with white arrows indicating the direction of line scans, whose data is presented in (d,h). Within EDX maps, red represents Fe and blue represents W.

Studies on fully crystalline NMs, such as Mo-Au [16] and Cu-W [34], reported key stages of multilayer breakdown that involved diffusion-mediated processes, including grooving and pinch-off. Notably, several multilayer studies have focused on complex non-metallic amorphous layers, where higher CAI density was shown to lower the critical temperature for layer breakdown [35,36]. Despite these observations, amorphous complexions and AIFs within fully metallic systems (e.g., Ni-W [17] and Cu-Zr-Hf [18] alloys) preserved nanocrystalline stability at temperatures over 1000 °C. Hence, a comprehensive understanding of the influence and evolution of amorphous metallic layers within multilayer structures is still limited. In this study, multilayer films were thermally aged at 500 °C where XRD results for monolithic amorphous-FeW samples exhibited significant differences in phase stability. Organized to mirror the as-sputtered film analysis, Fig. 3a and e show cross-sectional HAADF-STEM micrographs revealing the initial laminate structure remained intact after the 500 °C heat treatment. However, layer roughening was evident in Fe/Fe-38 W as shown in Fig 3b and EDX map in Fig. 3c. Faint white lines also span across several Fe layers, possibly indicating interlayer diffusion, which has been observed in multilayers consisting of miscible constituents [37].

Fe-W is commonly classified as a miscible (albeit low) system [38], and intermetallic formation is energetically favorable as formation enthalpies Fe-W compounds are negative [39]. Current understanding regarding how miscibility affects layer stability is largely based on systems with elemental and solid solution layers, such as Cu-Nb [40] and W-Cr [41]. Yet, prediction of laminate stability is not trivial, as coherency, grain size, homologous temperature, and composition all uniquely influence interface-driven mechanisms [42,43]. STEM and NBED images within Fig. 3b show clear diffraction spots from the Fe layer (red) and a diffuse ring from the Fe-38 W layer (blue), demonstrating retention of the amorphous state in the Fe-38 W phase. In contrast, NBED data in Fig. 3f for the Fe-67 W layer (blue) contains many diffraction spots indicating significant devitrification. Stability of Fe-38 W and Fe-67 W compositions within the multilayer samples follow the same pattern as the single-layer samples, with Fe-38 W remaining amorphous after heat-treatment and Fe-67 W devitrifying. Figs. 3c and 3 g display EDX maps of Fe (red) and W (blue) following the 500 °C heat treatment. Despite devitrification in Fe/Fe-67 W and interface blurring within Fe/Fe-38 W, both configurations retain distinguishable chemical layer interfaces. Line scan results presented in Figs. 3d and 3h reveal that Fe content alternates between 59 and 95 at.% for Fe/Fe-38 W and 33–91 at.% for Fe/Fe-67 W. Differences between as-sputtered and heat-treated line scan data are insignificant as they fall within the error of EDX capabilities, typically ±5 at.% [44]. Importantly, devitrification within Fe/Fe-67 W allows for the first time a direct comparison between laminate stability in systems containing metallic glass CAIs and

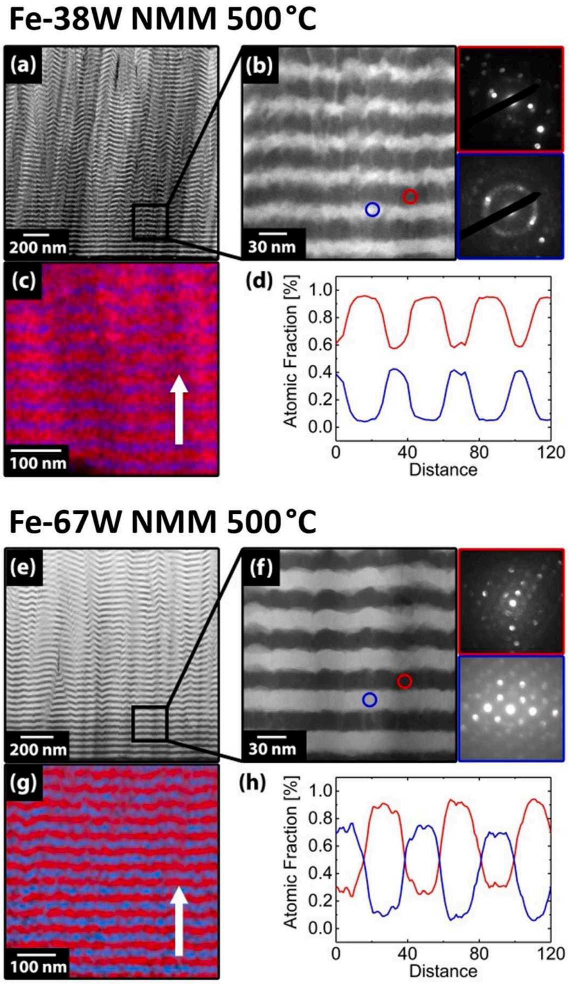

Fig. 3. Microstructural and chemical characterization of 500 °C treated (a-d) Fe-38 W multilayer and (e-h) Fe-67 W multilayer films. Microstructural analysis for both samples consists of (a,e) cross-sectional HAADF-STEM micrographs and (b,f) NBED scans with layer locations labeled within magnified STEM images. Chemical investigation consists of (c,g) EDX mapping of film cross sections with white arrows indicating the direction of line scans, whose data is presented in (d,h). Within EDX maps, red represents Fe and blue represents W.

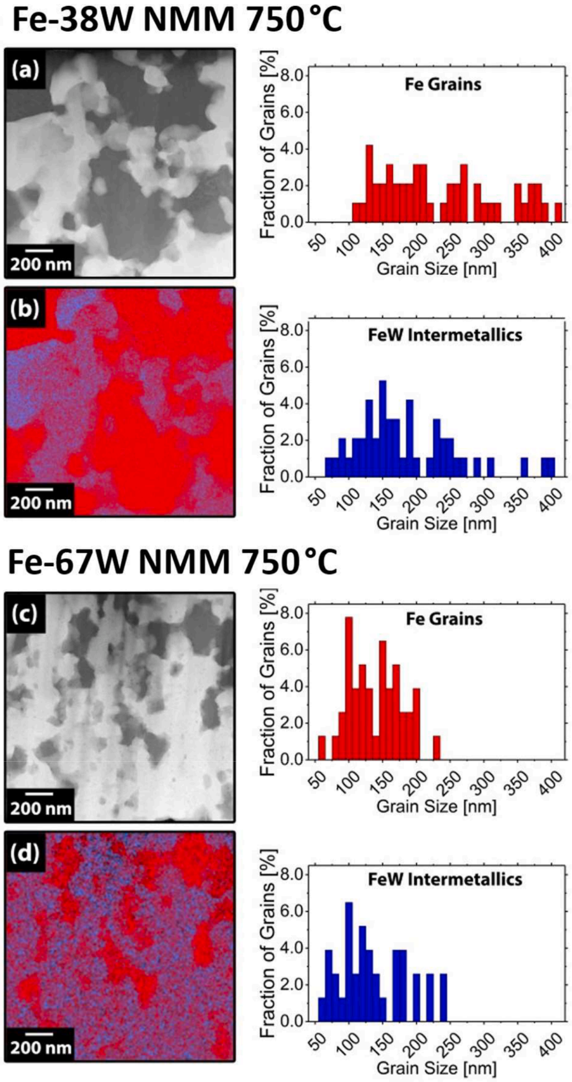

Fig. 4. Fe-38 W multilayer coatings are characterized after 750 °C treatment showing (a) a cross-sectional HAADF-STEM image and (b) EDX map displaying the microstructure after layer breakdown. Feature size histograms for Fe grains (red) and FeW-intermetallic phases (blue) are adjacent to STEM and EDX images. For the Fe-67 W multilayer coating, (c) and (d) represent similar STEM and EDX images respectively, with similar histograms depicting the distribution of each feature size. Within EDX maps, red represents Fe and blue represents W.

multilayers containing CCIs. Thus, differences in interfacial characteristics between Fe/Fe-38 W and Fe/Fe-67 W present a unique opportunity to explore interface-driven mechanisms within the same system beyond temperatures previously studied.

Given the onset of devitrification at 750 °C in the more stable Fe-38 W monolithic amorphous film in Fig. 1a, NM samples were thermally aged at this temperature for 96 h. Cross-sectional HAADF micrographs in Fig. 4 demonstrate both films experienced complete recrystallization of the multilayer structure. EDX shows separation between Fe grains (red) and FeW intermetallic phases (blue) where α-Fe and λ-Fe_2W are expected, per the Fe-W phase diagram [39]. Notably, the propensity for Fe_7W_6 formation as observed in the monolithic films is suppressed in the NM samples, since the overall Fe content is increased to where neither Fe_7W_6 nor BCC-W solution phases are expected. Counting over 75 grains for each sample, grain sizes for Fe and FeW-intermetallic phases within Fe/Fe-38 W are 240 ± 48 nm and 192 ± 47 nm respectively, whereas Fe and FeW-intermetallic phases within Fe/Fe-67 W are 145 ± 40 nm and 142 ± 50 nm. Because HAADF-STEM images primarily provide Z-contrast, it can be difficult to clearly distinguish grain boundaries which likely accounts for the broad distribution of measured grain sizes. Although Fe/Fe-67 W displays slightly smaller Fe and intermetallic features relative to Fe/Fe-38 W, both annealed samples exhibit nanoscale features about 200–1000 nm smaller than other nanostructured ferritic and W-based alloys [45,46].

Prior to recrystallization, interface-driven mechanisms influencing layer breakdown can be inferred by comparing Figs. 3 and 4. Within Fig. 3, Fe/Fe-38W's CAIs appear blurred indicating interlayer diffusion and mixing. Amorphous alloys have demonstrated significant excess free volume over crystalline counterparts, which is closely linked with accelerated diffusion [47]. For example, self-diffusivity in amorphous Fe-Zr was calculated to be 5–10 orders of magnitude larger than in crystalline Fe, though values are highly dependent on composition [48]. Thus, CAIs with miscible constituents, such as Fe and W, may be prone to layer breakdown via diffusion-driven interlayer mixing culminating in recrystallization into α-Fe and intermetallic-FeW phases. In contrast, in the Fe/Fe-67 W NM, the amorphous phase devitrified into Fe_2W and Fe_7W_6 intermetallic phases, resulting in Fe/intermetallic-FeW CCI interfaces. The evolution of metal/intermetallic interfaces is largely understood as a grooving mechanism, where the more thermally stable intermetallic layer grooves into the elemental layer leading to pinch off

[49]. Intermetallic grooving has been observed in metal/intermetallic laminates including Nb/Nb_5Si_3 [50] and Mo/$MoSi_2$ [51]. Interfacial free energy has been linked with nanocrystalline laminate stability, yet grain boundary free energies are not readily available for many intermetallic compounds [49]. Layer grooving is dependent on the solidus temperature of the intermetallic relative to the pure metal; solidus temperatures of Fe_2W and Fe_7W_6 are both reported to be 1637 °C [39], about 100 °C higher than the melting temperature of iron. As a result, Fe/Fe-67 W likely evolved via intermetallic formation within the Fe-67 W layer followed by interfacial grooving leading to pinch off and coarsening. After recrystallization, Fe/Fe-38 W shows a higher fraction of Fe grains relative to Fe/Fe-67 W, which consists of smaller and more numerous intermetallic grains. Importantly, thermal stability studies on nanocrystalline W-based alloys identified that precipitation can inhibit grain growth via interface pinning [52]. Thus, smaller feature sizes within Fe/Fe-67 W may be attributed to pinning effects imparted by nanoscale intermetallics.

Despite the differing layer breakdown mechanisms discussed, few microstructural differences are observed after the 750 °C treatment, as both films recrystallized into nanoscale microstructures consisting of Fe and Fe-W intermetallic phases. Ultimately, these findings are in contrast to recent work demonstrating that CAIs associated with AIFs can significantly improve the thermal stability of nanostructured materials [17,18,53]. However, direct comparison between intergranular films and multilayers is challenging, as CAIs' influence on thermal stability is highly dependent on the shape and size of amorphous and crystalline phases within a nanostructured system. In addition, AIFs and complexions were purported to be in thermal equilibrium with neighboring grains, whereas the co-sputtered amorphous-FeW phases in this study are metastable. Nevertheless, our results demonstrate that nanomultilayers can be tailored to serve as candidate systems for investigating interfacial characteristics such as CAIs and their influence on nanoscale stability for extreme environments.

Declaration of Competing Interest

The authors declare that they have no known competing financial interests or personal relationships that could have appeared to influence the work reported in this paper.

Acknowledgments

This work was performed under the auspices of the Department of Energy under Grant DE-SC0021060 as well as the Deutsche Forschungsgemeinschaft under Grant 426206394. We acknowledge the Core Center of Excellence in Nano Imaging at USC.

References

[1] A. Sáenz-Trevizo, A.M. Hodge, Nanomaterials by design: a review of nanoscale metallic multilayers, Nanotechnology 31 (29) (2020), 292002.
[2] S. Wurster, R. Pippan, Nanostructured metals under irradiation, Scr. Mater. 60 (12) (2009) 1083–1087.
[3] C.D. Appleget, J.S. Riano, A.M. Hodge, An overview of nano multilayers as model systems for developing nanoscale microstructures, Materials (2022) (Basel).
[4] J.A. Bahena, J. Sebastian Riano, M.R. Chellali, T. Boll, A.M. Hodge, Thermally activated microstructural evolution of sputtered nanostructured Mo–Au, Materials 4 (2018) 157–165.
[5] N. Figueiredo-Prestes, J. Zarpellon, D.d.S. Costa, I. Mazzaro, P.C. de Camargo, A. J. de Oliveira, C. Deranlot, J.M. George, D.H. Mosca, Thermal Stability of Ultrathin Co/Pt Multilayers, J. Phys. Chem. C 125 (8) (2021) 4885–4892.
[6] J.L. Qi, L.P. Wang, Y. Zhang, X. Guo, W.Q. Yu, Q.H. Wang, K. Zhang, P. Ren, M. Wen, Amorphous AlN nanolayer thickness dependent toughness, thermal stability and oxidation resistance in TaN/AlN nanomultilayer films, Surf. Coat. Technol. 405 (2021), 126724.
[7] E.G. Bauer, B.W. Dodson, D.J. Ehrlich, L.C. Feldman, C.P. Flynn, M.W. Geis, J. P. Harbison, R.J. Matyi, P.S. Peercy, P.M. Petroff, J.M. Phillips, G.B. Stringfellow, A. Zangwill, Fundamental issues in heteroepitaxy—A department of energy, council on materials science panel report, J. Mater. Res. 5 (4) (1990) 852–894.
[8] J. Weissmüller, Alloy thermodynamics in nanostructures, J. Mater. Res. 9 (1) (2011) 4–7.
[9] M. Wagih, C.A. Schuh, Thermodynamics and design of nanocrystalline alloys using grain boundary segregation spectra, Acta Mater. 217 (2021), 117177.
[10] W. Xing, A.R. Kalidindi, D. Amram, C.A. Schuh, Solute interaction effects on grain boundary segregation in ternary alloys, Acta Mater. 161 (2018) 285–294.
[11] A.R. Kalidindi, C.A. Schuh, Stability criteria for nanocrystalline alloys, Acta Mater. 132 (2017) 128–137.
[12] O.K. Donaldson, W. Wang, K. Hattar, J.R. Trelewicz, Impurity stabilization of nanocrystalline grains in pulsed laser deposited tantalum, J. Mater. Res. 32 (7) (2017) 1351–1360.
[13] N. Olynik, B. Cheng, D.J. Sprouster, C.M. Parish, J.R. Trelewicz, Microstructural transitions during powder metallurgical processing of solute stabilized nanostructured tungsten alloys, Metals 12 (1) (2022) 159 (Basel).
[14] T. Lei, J. Shin, D.S. Gianola, T.J. Rupert, Bulk nanocrystalline Al alloys with hierarchical reinforcement structures via grain boundary segregation and complexion formation, Acta Mater. 221 (2021), 117394.
[15] X. Zhou, A. Gupta, G.J. Tucker, G.B. Thompson, Manipulation of solute partitioning mechanisms for nanocrystalline stability, Acta Mater. 208 (2021), 116662.
[16] W.S. Cunningham, S.T.J. Mascarenhas, J.S. Riano, W. Wang, S. Hwang, K. Hattar, A.M. Hodge, J.R. Trelewicz, Unraveling thermodynamic and kinetic contributions to the stability of doped nanocrystalline alloys using nanometallic multilayers, Adv. Mater. 34 (27) (2022).
[17] O.K.D. Jennifer, D. Schuler, Timothy J. Rupert, Amorphous complexions enable a new region of high temperature stability in nanocrystalline Ni-W, Scr. Mater. 154 (2018).
[18] C.M. Grigorian, T.J. Rupert, Thick amorphous complexion formation and extreme thermal stability in ternary nanocrystalline Cu-Zr-Hf alloys, Acta Mater. 179 (2019) 172–182.
[19] G.H. Balbus, J. Kappacher, D.J. Sprouster, F. Wang, J. Shin, Y.M. Eggeler, T. J. Rupert, J.R. Trelewicz, D. Kiener, V. Maier-Kiener, D.S. Gianola, Disordered interfaces enable high temperature thermal stability and strength in a nanocrystalline aluminum alloy, Acta Mater. 215 (2021), 116973.
[20] T. Jennifer D. Schuler, J. Rupert, Materials selection rules for amorphous complexion formation in binary metallic alloys, Acta Mater. 140 (2017).
[21] J.D. Schuler, C.M. Grigorian, C.M. Barr, B.L. Boyce, K. Hattar, T.J. Rupert, Amorphous intergranular films mitigate radiation damage in nanocrystalline Cu-Zr, Acta Mater. 186 (2020) 341–354.
[22] X. Zhang, K. Hattar, Y. Chen, L. Shao, J. Li, C. Sun, K. Yu, N. Li, M.L. Taheri, H. Wang, J. Wang, M. Nastasi, Radiation damage in nanostructured materials, Prog. Mater. Sci. 96 (2018) 217–321.
[23] T. Yue, Y.Q. Wang, J.Y. Zhang, K. Wu, G. Li, J. Kuang, G. Liu, J. Sun, Unraveling the discrepancies in size dependence of hardness and thermal stability in crystalline/amorphous nanostructured multilayers: cu/Cu–Ti vs. Cu/HfO2, Nanoscale 10 (29) (2018) 14331–14341.
[24] M. Lu, C.L. Chien, Structural and magnetic properties of Fe-W alloys, J. Appl. Phys. 67 (9) (1990) 5787–5789.
[25] E. Pekarskaya, J.F. Löffler, W.L. Johnson, Microstructural studies of crystallization of a Zr-based bulk metallic glass, Acta Mater. 51 (14) (2003) 4045–4057.
[26] L.T. Chen, J.W. Lee, Y.C. Yang, B.S. Lou, C.L. Li, J.P. Chu, Microstructure, mechanical and anti-corrosion property evaluation of iron-based thin film metallic glasses, Surf. Coat. Technol. 260 (2014) 46–55.
[27] M.N. Avettand-Fènoël, M. Marinova, R. Taillard, W. Jiang, Thermal stability, phase transformations and mechanical properties of a Fe64B24Y4Nb6 metallic glass, J. Alloy. Compds. 854 (2021), 157068.
[28] C. Popov, W. Kulisch, S. Boycheva, K. Yamamoto, G. Ceccone, Y. Koga, Structural investigation of nanocrystalline diamond/amorphous carbon composite films, Diam. Relat. Mater. 13 (11) (2004) 2071–2075.
[29] M. Apreutesei, P. Steyer, L. Joly-Pottuz, A. Billard, J. Qiao, S. Cardinal, F. Sanchette, J.M. Pelletier, C. Esnouf, Microstructural, thermal and mechanical behavior of co-sputtered binary Zr–Cu thin film metallic glasses, Thin Solid Films 561 (2014) 53–59.
[30] A. Antoni-Zdziobek, T. Commeau, J.M. Joubert, Partial redetermination of the Fe-W phase diagram, Metal. Mater. Trans. A 44 (7) (2013) 2996–3003.
[31] H. Okamoto, Supplemental literature review of binary phase diagrams: b-Fe, Cr-Zr, Fe-Np, Fe-W, Fe-Zn, Ge-Ni, La-Sn, La-Ti, La-Zr, Li-Sn, Mn-S, and Nb-*Re*, J. of Ph. Equilib. Diff. 37 (5) (2016) 621–634.
[32] N. Tsyntsaru, J. Bobanova, X. Ye, H. Cesiulis, A. Dikusar, I. Prosycevas, J.P. Celis, Iron–tungsten alloys electrodeposited under direct current from citrate–ammonia plating baths, Surf. Coat. Technol. 203 (20) (2009) 3136–3141.
[33] D.B. Miracle, D.V. Louzguine-Luzgin, L.V. Louzguina-Luzgina, A. Inoue, An assessment of binary metallic glasses: correlations between structure, glass forming ability and stability, Int. Mater. Rev. 55 (4) (2010) 218–256.
[34] F. Moszner, C. Cancellieri, M. Chiodi, S. Yoon, D. Ariosa, J. Janczak-Rusch, L.P. H. Jeurgens, Thermal stability of Cu/W nano-multilayers, Acta Mater. 107 (2016) 345–353.
[35] Q. Su, M. Zhernenkov, H. Ding, L. Price, D. Haskel, E.B. Watkins, J. Majewski, L. Shao, M.J. Demkowicz, M. Nastasi, Reaction of amorphous/crystalline SiOC/Fe interfaces by thermal annealing, Acta Mater. 135 (2017) 61–67.
[36] Y. He, X. Wang, T. Guo, K. Gao, X. Pang, Crystal interface-enhanced thermal stability of CrAlN/SiNx multilayer films, Surf. Coat. Technol. 445 (2022), 128725.
[37] H. Wan, Y. Shen, X. He, J. Wang, Modeling of microstructure evolution in metallic multilayers with immiscible constituents, J. Min. Mater. Met 65 (3) (2013) 443–449.
[38] R.F. Zhang, X.F. Kong, H.T. Wang, S.H. Zhang, D. Legut, S.H. Sheng, S. Srinivasan, K. Rajan, T.C. Germann, An informatics guided classification of miscible and immiscible binary alloy systems, Sci. Rep. 7 (1) (2017) 9577.

[39] A. Jacob, C. Schmetterer, L. Singheiser, A. Gray-Weale, B. Hallstedt, A. Watson, Modeling of Fe–W phase diagram using first principles and phonons calculations, Calphad 50 (2015) 92–104.

[40] C. Ding, J. Xu, D. Shan, B. Guo, T.G. Langdon, The thermal instability mechanism and annealed deformation behavior of Cu/Nb nanolaminate composites, J. Mater. Sci. Technol 157 (2023) 163–173.

[41] J.S. Riano, A.M. Hodge, Phase transformations in the W–Cr system at the nanoscale, Materials 2 (2018) 190–195.

[42] I.J. Beyerlein, J. Wang, Interface-driven mechanisms in cubic/noncubic nanolaminates at different scales, MRS Bull. 44 (1) (2019) 31–39.

[43] I.J. Beyerlein, M.J. Demkowicz, A. Misra, B.P. Uberuaga, Defect-interface interactions, Prog. Mater. Sci. 74 (2015) 125–210.

[44] D.E. Newbury*, N.W.M. Ritchie, Is Scanning Electron microscopy/energy dispersive X-ray spectrometry (SEM/EDS) quantitative? Scanning 35 (3) (2013) 141–168.

[45] H. Kurishita, S. Matsuo, H. Arakawa, T. Sakamoto, S. Kobayashi, K. Nakai, H. Okano, H. Watanabe, N. Yoshida, Y. Torikai, Y. Hatano, T. Takida, M. Kato, A. Ikegaya, Y. Ueda, M. Hatakeyama, T. Shikama, Current status of nanostructured tungsten-based materials development, Phys. Scr. (T159) (2014), 014032, 2014.

[46] G.R. Odette, On the status and prospects for nanostructured ferritic alloys for nuclear fission and fusion application with emphasis on the underlying science, Scr. Mater. 143 (2018) 142–148.

[47] A. Heesemann, K. Rätzke, V. Zöllmer, F. Faupel, Does the diffusion mechanism in thin amorphous Co81Zr19 films change during structural relaxation? New J. Phys. 3 (1) (2001) 306.

[48] W. Frank, J. Horváth, H. Kronmüller, Diffusion mechanisms in amorphous alloys, Mater. Sci. Eng 97 (1988) 415–418.

[49] A.C. Lewis, D. Josell, T.P. Weihs, Stability in thin film multilayers and microlaminates: the role of free energy, structure, and orientation at interfaces and grain boundaries, Scr. Mater. 48 (8) (2003) 1079–1085.

[50] H. Cao, J.P.A. Löfvander, A.G. Evans, R. Grant Rowe, D.W. Skelly, Mechanical properties of an *in situ* synthesized Nb/Nb3Al layered composite, Mat. Sci. Eng. A 185 (1) (1994) 87–95.

[51] R.G. Rowe, D.W. Skelly, M. Larsen, J. Heathcote, G.R. Odette, G.E. Lucas, Microlaminated high temperature intermetallic composites, Scr. Metal. Mater. 31 (11) (1994) 1487–1492.

[52] C.C. Koch, R.O. Scattergood, M. Saber, H. Kotan, High temperature stabilization of nanocrystalline grain size: thermodynamic versus kinetic strategies, J. Mater. Res. 28 (13) (2013) 1785–1791.

[53] A. Khalajhedayati, T.J. Rupert, High-Temperature Stability and Grain Boundary Complexion Formation in a Nanocrystalline Cu-Zr Alloy, J. Min. Mater. Met. Soc. 67 (12) (2015) 2788–2801.